Plasma exosomes from individuals with type 2 diabetes drive breast cancer aggression in patient-derived organoids

Christina S. Ennis[1], Michael Seen[1], Andrew Chen[2,3], Heejoo Kang[1], Adrian Ilinski[4], Kiana Mahdaviani[4], Naomi Ko[4], Stefano Monti[2,3,5], Gerald V. Denis[1,4,6]

[1]Cancer Center, Boston University Chobanian and Avedisian School of Medicine, Boston, Massachusetts, USA

[2]Department of Medicine, Computational Biomedicine Section, Boston University Chobanian and Avedisian School of Medicine, Boston, Massachusetts, USA

[3]Bioinformatics Program, Faculty in Computing and Data Science, Boston University, Boston, Massachusetts, USA

[4]Section of Hematology/Oncology, Department of Medicine, Boston University Chobanian and Avedisian School of Medicine, Boston, Massachusetts, USA

[5]Department of Biostatistics, Boston University School of Public Health, Boston, Massachusetts, USA

[6]Department of Pharmacology and Experimental Therapeutics, Boston University Chobanian and Avedisian School of Medicine, Boston, Massachusetts, USA

Running title. T2D exosomes drive breast cancer aggression in PDOs.

Corresponding Author. Gerald V Denis, Boston University Chobanian and Avedisian School of Medicine School of Medicine, 72 East Concord Street, Rm K408, Boston, MA 02118 Phone: 617-414-1371, Lab: 617-414-1372, Fax 617-638-5673; E-mail: gdenis@bu.edu

Conflict of interest. The authors affirm that they have no conflicts to disclose.

Grant Support. This work was supported by grants from NIH: U01CA182898, U01CA243004 and R01CA222170 to G.V. Denis; 5T32AI007309 (PI: Gummurulu) to C.S. Ennis.

Word count, excluding references: 5176

Figures: 7

References: 70

Abstract

Women with obesity-driven diabetes (T2D) are predisposed to more aggressive breast cancers, yet patient metabolic status does not fully inform current standards of care. We previously identified plasma exosomes as key mediators of intercellular communication and drivers of tumor progression; however, their effect on immune cells within the tumor microenvironment (TME) remains unclear. To model this exosomal signaling, we developed a novel method to generate patient-derived organoids (PDOs) from breast tumor resections, uniquely preserving native tumor-infiltrating lymphocytes (TILs) for the first time. This modifiable and reproducible system provides a robust platform for studying human tumor-immune interactions within the TME *in vitro*. After 3-day exosome treatment, we assessed the impact of T2D-derived exosomes on PDOs via single-cell RNA sequencing. Exosomes from T2D patient plasma triggered a 13.6-fold expansion of immunosuppressive TILs compared to non-diabetic exosome controls. This immune dysfunction may permit the survival of micrometastases and undermine immune checkpoint therapies, a known challenge for cancer patients with comorbid T2D. Tumor-intrinsic analysis revealed a 1.5-fold increase in intratumoral heterogeneity and approximately 2.3-fold upregulation of epithelial-to-mesenchymal transition, invasiveness, and cancer stemness, consistent with enhanced tumor aggressiveness and metastatic potential of these PDOs. These findings demonstrate how metabolic dysregulation in T2D disrupts tumor-immune crosstalk, profoundly impairing anti-tumor immunity and driving cancer progression through a previously underappreciated exosomal signaling pathway. These insights into the TME could inform personalized treatments for patients with this comorbidity.

(232 words)

50 ## Introduction

51 Metabolic disorders, particularly Type 2 diabetes (T2D), raise concerns for the management of
52 breast cancer. Population studies have shown that women with T2D have 40% increased risk of developing
53 breast cancer and 74% increase in overall mortality compared to non-diabetic (ND) women[1]. The alarming
54 impact of this comorbidity underscores a critical gap in our understanding of the cellular and molecular
55 mechanisms linking these diseases. Recently, investigations into the immune phenotype of T2D have
56 described subclinical chronic inflammation that induces insulin resistance and metabolic dysfunction that
57 accompany the disease[2]. This inflammatory milieu ultimately leads to T cell dysfunction[3], posing a
58 significant clinical challenge for breast cancer patients. Cancer cells have adaptations that allow them to
59 exploit this dysfunction, reprogramming immune cells to evade detection and clearance[4]. Traditional
60 molecular diagnostics fall short in capturing these profound differences seen in the tumor
61 microenvironment (TME) of T2D[1], highlighting an urgent need for improved diagnostic and therapeutic
62 approaches. Here, we use novel models to focus on unique features of this TME to explore mechanisms
63 that may contribute significantly to breast cancer progression in T2D.

64 Within the breast TME, exosomes have emerged as key mediators of cellular communication.
65 Initially dismissed as mere cellular disposal systems, these nano-sized extracellular vesicles are now
66 recognized for their crucial roles in transferring bioactive molecules, such as proteins, lipids, and nucleic
67 acids, between cells that influence tumor behavior and progression[5]. Our group and others have recently
68 highlighted the critical role of exosomes in linking metabolic dysregulation with cancer pathophysiology[5–
69 7]. We demonstrated that exosomes isolated from T2D patient adipocytes promote a more aggressive tumor
70 phenotype in cellular models of breast cancer, increasing epithelial-to-mesenchymal transition (EMT) and
71 cancer stem-like cell (CSC) formation, compared to ND controls[8]. Similarly, plasma-derived exosomes
72 from T2D patients enhanced EMT and CSC traits in prostate cancer cell lines[9]. Furthermore, T2D
73 exosomes carry distinctive biomarkers that could serve as diagnostic or prognostic tools[5,9], and offer new
74 insights into the intercellular communication of the TME that drives breast cancer progression in

metabolic disorders. However, these studies have yet to fully elucidate how exosomal treatment affects other cell types of the TME, and how this might exacerbate overall tumor aggressiveness.

Accurate modeling of the TME presents a challenge due to its intricate and dynamic cellular interactions. Recent advances in three-dimensional *in vitro* systems, such as patient-derived organoids (PDOs), have started to bridge this gap by preserving the heterogeneity and architecture of the originating tumors[10,11]. Leveraging this model, coupled with advancements in single-cell RNA sequencing - although sparingly used in breast cancer PDO research - have been instrumental in detailing the landscape of intratumoral heterogeneity preserved in PDOs[12]. However, a significant limitation has been the attrition and eventual elimination of the immune fraction[13]. Our novel approach enhances standard breast cancer PDO models by successfully preserving and comprehensively profiling native, primary breast tumor-infiltrating lymphocytes (TILs), for the first time to our knowledge. This advancement is a significant stride in breast cancer research, as it allows for a more accurate study of the immune-tumor interactions within the TME.

Here, we explore how exosomes derived from T2D patient plasma increase the aggressiveness of breast cancer. We hypothesize that T2D plasma-derived exosomes promote oncogenic processes, including EMT, CSC formation, and immune evasion, within the PDO model. Elucidating these interactions will refine our understanding of the role of T2D in breast cancer progression, offering novel insights that could fundamentally alter clinical approaches to breast cancer treatment.

Results

Single-cell RNA sequencing reveals cellular landscape of PDOs

To elucidate the cellular architecture and explore the effects of exosomal communication in breast cancer, we developed a robust *in vitro* model using PDOs generated from estrogen receptor-positive breast tumor resection samples from three ND patients (Fig. 1A, Table S1). Briefly, tumor tissues were mechanically and enzymatically digested with collagenase, and the resulting cell clusters were embedded in a basement membrane extract (BME) and cultured with a cocktail of growth factors to support organoid

101 formation and maintain native TME populations and their neighborhood architecture. PDOs were then
102 treated with plasma-derived exosomes from two carefully selected patients to minimize experimental
103 variability: an ND individual (ND*exo*-PDOs) and a patient with T2D (T2D*exo*-PDOs, glycated
104 hemoglobin (HbA1c) 9.3%). These donors were chosen based on a preliminary screen of 15 patients,
105 selecting those that would maximize the detection of functional differences in TME behavior. This
106 approach ensured consistent experimental conditions across different PDO batches and facilitated a
107 focused examination of how metabolic status influences TME dynamics. Plasma exosomes were isolated
108 from EDTA-anticoagulated, peripheral venous blood, and quantified to deliver 5,000 particles per PDO
109 cell. A control group of untreated PDOs (UT-PDOs) was maintained to establish a baseline for
110 comparison.

111 After stringent quality control (see Methods), we obtained transcriptomes of 24,599 single cells
112 across three independently generated PDO lines each under three conditions, UT, ND*exo*, and T2D*exo*
113 subjected to exosome treatment (Fig. 1B-D, 318: UT - n = 2007, ND*exo* - n = 2384, T2D*exo* - n = 2562;
114 377: UT - n = 5396, ND*exo* - n = 6915, T2D*exo* - n = 4953; 409: UT - n = 164, ND*exo* - n = 124, T2D*exo*
115 - n = 94). The samples were integrated computationally using single-cell variational inference (scVI)[14] to
116 address interpatient variability of tumor cell fractions (Fig. S1A-B). Copy number alterations were used
117 to distinguish neoplastic from normal cells, leveraging immune cells also captured within PDOs (Fig. 1E,
118 Fig. S2A-C). Tumor cell identities were validated by comparing gene expression profiles of breast cancer-
119 specific gene sets from the Catalogue of Somatic Mutations in Cancer (COSMIC) Cancer Gene Census
120 (CGC)[15] and gene sets related to mammary epithelial proliferation[16] (Fig. S1C).

121 Unsupervised uniform manifold approximation and projection (UMAP)-clustering revealed 17
122 clusters, which were further classified via automatic cell annotation[17,18] and established lineage-specific
123 marker genes (Fig. 1F, Fig. S1D, Table S2). Notably, many crucial cell types were abundantly present
124 across all patient samples (Fig. 1C). We identified 20,173 epithelial cells, which accounted for the majority
125 of sequenced cells. We identified three major stromal cell types (Fig. 1B) including cancer associated
126 fibroblasts (CAFS; *FAP, COL1A1*), perivascular-like cells (PVL; *PDGFRA, PDGFRB*), and endothelial

127 cells (*PECAM1, CD34*). Critically, we identified distinct clusters relating to various immune cell types,
128 including T cells (*CD3E, CD8A*), B cells (*MS4A1, PAX5*), and macrophages (*CD68, CD163*).

129 While PDO318 showed lower immune cell abundance compared to PDO377 and PDO409, the
130 variation observed across the three PDOs likely reflects real interpatient differences in tumor-immune
131 composition—a feature well-documented in breast cancer[18–20]. To contextualize these findings, we
132 benchmarked our data against our recently assembled breast cancer single cell atlas[21], confirming that the
133 cellular proportions in our PDOs fall within the spectrum observed in primary breast tumors (Fig. S1E).
134 To control for variability across PDO lines, we explicitly model patient batch as a latent variable in our
135 statistical framework. This approach, in which tumor, stromal, and immune populations are preserved in
136 PDOs, represents a substantial advancement over traditional methods, which fail to maintain native breast
137 TIL populations, and provides a comprehensive platform for studying immune-tumor interactions in breast
138 cancer.

139

140 **T2D*exo*-PDOs exhibit aggressive phenotypes, compared to ND*exo*-PDOs**

141 To elucidate the distinct transcriptional impacts of T2D-exosomal communication, we conducted
142 gene set enrichment analysis (GSEA)[22] on differentially expressed genes across all cell populations (Table
143 S3). All changes we report were statistically significant. T2D*exo*-PDOs showed 2.1-fold upregulation of
144 pathways related to EMT, invasiveness, and stemness compared to nondiabetic controls (Fig. 2A-B). This
145 fold change was based on the normalized enrichment score from differential expression analysis. These
146 hallmark processes are associated with aggressive tumor phenotypes and metastatic potential, consistent
147 with our previous findings that T2D exosomes promote tumorigenic reprogramming in breast cancer
148 models[8].

149 Validation of these findings was further supported by the upregulation of breast cancer genes listed
150 in the COSMIC CGC and canonical CSC markers within the T2D*exo*-treated epithelial cell fraction
151 compared to ND*exo*-PDOs (Fig. 2C). Top differentially expressed genes include well known drivers of
152 aggressiveness and stemness (Fig. 2D, Table S4; *NOTCH1, MMP14*). These results align with our prior

153 PCR-validated data[8], strengthening the evidence that T2D exosomes promote aggressive cancer
154 phenotypes. Morphological assessments of PDOs supported these findings, with T2D*exo*-PDOs
155 displaying pronounced budding (Fig. 2E-F, Table S5), a morphological indicator of increased metastatic
156 capacity[23]. Such findings are consistent with our previous reports of T2D exosomes promoting migration
157 and morphological changes in other cellular models[8,9,24], further reinforcing their role in enhancing tumor
158 aggressiveness.

159 Conversely, ND*exo*-PDOs demonstrated 3.6-fold activation of T cell mediated immune responses
160 (Fig. 2A,C-D, Table S3). Specifically, pathways related to antigen binding and presentation, along with
161 cytotoxic T cell signaling, were upregulated 3.9-fold and 3.3-fold, respectively, in ND*exo* relative to
162 T2D*exo*-PDOs, indicating enhanced tumor immunogenicity and immune system recognition.

163 To evaluate the broader relevance of these findings, we generated a composite signature
164 representing the net transcriptional imprint of diabetes-associated exosomal signaling. We applied this
165 signature to two independent breast cancer cohorts—the cancer genome atlas (TCGA)[25] and the Molecular
166 Taxonomy of Breast Cancer International Consortium (METABRIC)[26] —and assessed its association with
167 overall survival, adjusting for age, proliferation score, inflammation score, and PAM50 subtype.
168 Strikingly, this signature was associated with significantly worse survival outcomes in both datasets (Fig.
169 2G, Table S6; TCGA: HR = 2.23, $p < 0.002$; METABRIC: HR = 2.06, $p < 1.2e-05$), underscoring its
170 clinical relevance and generalizability beyond our in vitro system.

171 Functional annotation further revealed distinct biological programs: the T2D-like gene set was
172 enriched for pro-tumorigenic pathways, including genes related to metabolism (26.5%),
173 transcription/signaling (19.1%), invasion/EMT/proliferation (16.2%), ECM remodeling (11.8%), and
174 stemness/development (7.4%). Only 5.9% of T2D-like genes were immune-related, half of which were
175 suppressive. In contrast, the ND-like gene set was 91.4% immune-enriched, with dominant roles in T cell
176 activation (30.6%), leukocyte migration (18.8%), and T cell development (16.5%)—features indicative of
177 an anti-tumor immune phenotype.

178 These results reinforce epidemiologic findings that T2D is associated with worse breast cancer
179 outcomes[27,28] and demonstrate that diabetes-linked exosomal programs can be linked to clinically
180 meaningful survival differences. While TCGA and METABRIC do not include metabolic status metadata,
181 this limitation highlights the unique value of our model in systematically linking systemic metabolic
182 disease to tumor-intrinsic transcriptional states.
183
184 **Exosomes from T2D plasma increase intratumoral heterogeneity**
185 Given the predominance of epithelial cells in our dataset, we next analyzed epithelial lineage-
186 specific responses within T2D*exo*-PDOs versus ND*exo*-PDOs. We identified 11 distinct cell clusters (Fig.
187 3A-B, Table S7), representing typical epithelial cell types, including normal luminal epithelial (LEC;
188 *KRT18*), myoepithelial (MEC; *TAGLN, KRT14*), and cycling cells (CYC; *MKI67, TOP2A*).
189 Malignant cells were further classified into two distinct groups: luminal-like and basal-like. The
190 luminal-like group consisted of five clusters (LT1-5), defined by *ESR1* positivity and expression of
191 *KRT19*, whereas the basal-like group comprised two clusters (BT1-2) characterized by *ESR1* negativity
192 and expression of canonical basal markers (*KRT5, VIM*). Despite all patients being clinically diagnosed
193 as estrogen receptor-positive, our data, consistent with other studies[18], highlighted subtype mixing within
194 individual tumors that was faithfully recapitulated in PDOs. In addition to these clearly malignant clusters,
195 we identified a population of luminal progenitor-like cells (LP; *KIT, ELF5*), which are considered the
196 presumptive cells of origin for breast cancer and are indicative of cancer stemness[18].
197 In the luminal-like group, we identified five subtypes (Table S7). Clusters LT1 and LT2 showed
198 high expression of genes associated with energy metabolism and oxidative stress (*MALAT1, NDUFC2,*
199 *ELOB*). LT3 exhibited a heightened proliferation index, indicated by increased expression of *MKI67* and
200 *TOP2A*, and genes marking breast epithelium (*ANKRD30A*). Importantly, whereas this cluster expressed
201 proliferation-associated genes, it did not exhibit the same transcriptional profile as actively cycling cells,
202 which clustered separately. This result suggests that LT3 represents a less proliferative, and potentially
203 less aggressive, tumor subpopulation. LT4 was characterized by genes linked to increased immune

204 infiltration (*HLA-A, B2M*). LT5 showed upregulation of genes associated with poor clinical outcomes
205 (*MUC1, SERPINA3*). Within the basal-like fraction, most cells belonged to the BT1 cluster, marked by
206 the expression of hallmark aggressive genes (*VIM, ITGA6*). Conversely, BT2 was characterized by genes
207 associated with a protein synthesis phenotype (*RPS15*).

208 To probe how exosome treatment impacted luminal-like tumor cell niches, we conducted a
209 differential proportion analysis of tumor clusters. We observed 1.5-fold expansion of the LT1 cluster,
210 coupled with 2.2-fold contraction of LT3 in T2D*exo* compared to ND*exo*-PDOs (Fig. 3C, Fig. S3A-B).
211 These fold changes were calculated by comparing the proportion of epithelial cells belonging to each
212 cluster within each treatment group. LT1 marker gene analysis by GSEA revealed enrichment of gene sets
213 related to transcriptional plasticity and vesicle trafficking, including RNA polymerase complex binding
214 and phosphatidylinositol-3-phosphate biosynthesis (Fig. 3D, Table S8), consistent with increased
215 endocytic activity and potential responsiveness to exosome cargo. Surprisingly, we also observed
216 enrichment of gene sets composed of predicted targets of miRNAs enriched in T2Dexo (Fig. S3C-D),
217 including miR-374a, which we previously identified as significantly upregulated in T2D-derived
218 exosomes[9]. While this might initially suggest upregulation of miRNA targets, we interpret this enrichment
219 as a broader regulatory signature rather than direct target activation, potentially reflecting compensatory
220 or indirect responses to miRNA exposure within LT1.

221 To directly evaluate the impact of T2D*exo*-delivered miRNAs, we performed miRNA target
222 enrichment across all LT clusters. Targets of validated T2D-associated miRNAs[9] (miR-374a-5p, miR-93-
223 5p, let-7b-3p) were significantly enriched among genes downregulated in T2Dexo-treated LTs compared
224 to NDexo (Fig. 3E, Fisher's exact test, $p < 2.2 \times 10^{-16}$; odds ratio = 3.6), consistent with canonical miRNA-
225 mediated repression and providing strong evidence of functional miRNA activity in this context.

226 Consistent with prior findings[9,24], we observed upregulation of MMPs across all T2D*exo* cells (Fig.
227 2D, *MMP2, MMP14*). In parallel, we found downregulation of key MMP inhibitors, including *TIMP2* and
228 *LACTB*, specifically within T2D*exo* LT clusters (Fig. 3F). Both inhibitors are predicted or validated targets
229 of T2D-enriched miRNAs (*TIMP2* by miR-93-5p; *LACTB* by miR-374a), suggesting that luminal-like

230 tumor cells may be key sites of miRNA-driven repression that contributes to broader MMP activation.
231 These findings support a model in which T2D-derived exosomes promote pro-invasive signaling across
232 the TME.
233
234 **Exosome treatment accelerates tumor cell evolution**
235 To examine the evolutionary shifts induced by exosome treatment, we performed pseudotime
236 analysis[29] on the luminal-like epithelial cell fraction in PDOs, excluding basal-like epithelial, immune,
237 stromal, and cycling populations. Ordering these cells in pseudotime revealed a principal trajectory from
238 normal LECs to more transformed states. Notably, cells from T2D*exo*-PDOs were positioned significantly
239 later in pseudotime compared to those from ND*exo* or UT-PDOs (Fig. 4A), indicating that T2D plasma-
240 derived exosomes promote substantial evolution in tumor cell phenotypes. Overlaying tumor subclones
241 onto the pseudotime trajectory (Fig. S4A) revealed that the LT1 subclone was positioned furthest along
242 in pseudotime. This finding correlates with a higher proportion of LT1 cells in T2D*exo*-PDOs, potentially
243 explaining their advanced pseudotime positioning.
244 To delineate the specific evolutionary paths captured by pseudotime, we performed differential
245 gene expression using graph-autocorrelation. All changes we report were statistically significant. This
246 analysis revealed upregulation of oncogenic genes (Table S9; *MKI67, MMP2, PTMA*) along the trajectory
247 (Fig. 4B). Conversely, major histocompatibility complex (MHC) class I molecules (*HLA-A, HLA-B, HLA-*
248 *C*) were progressively downregulated, a common immune evasive strategy by cancer cells to thwart
249 immune detection and clearance[30]. Grouping these differentially expressed genes into co-regulated
250 modules resulted in eight distinct clusters (Fig. 4C). Importantly, module 5, which showed an increased
251 expression through pseudotime (Fig. S4B-C, Table S10), was upregulated in T2D*exo*-PDOs compared to
252 ND*exo* or UT-PDOs (Fig. 4D). Functional enrichment analysis using the Database for Annotation,
253 Visualization, and Integrated Discovery (DAVID) resource[31] revealed that this module is involved in EMT
254 (*CTNNB1, TRIM28, BRD2*), RNA splicing (*SNRNP70, SRSF4*), and aerobic metabolism (*ATP5F1A, MT-*
255 *ND5*) which are well known to be perturbed in T2D[1,32]. These findings are consistent with our previous

256 reports where treatment of MCF7 cells with T2D-derived exosomes induced shifts in metabolic
257 pathways[8].
258
259 **T2D*exo*-PDOs display enhanced immune evasion through T cell dysfunction**
260 Given the significant downregulation of T cell signaling, we conducted a focused analysis of the
261 immune cell compartment within T2D*exo*-PDOs compared to ND*exo*-PDOs. We identified 10 distinct
262 cell clusters representing 1,760 various immune cells (Fig. 5A-B, Table S11) upon reclustering, including
263 T cells (*CD3E, TRAC)*, B cells (*MS4A1, CD79A*), plasma cells (*MZB1, SDC1*), and macrophages (*CD68,*
264 *CD163*).
265 T cells were further classified into six distinct subsets. The largest proportion consisted of memory
266 T cells, including central memory (Tcm; *SELL, CCR7*) and effector memory T cells (Tem; *SELL-, CCR7-*
267). We also identified clear populations of active anti-tumorigenic T cell states, including effector T (Teff;
268 *CD8A, GZMB*) and T helper 1 cells (Th1; *CD4, IFNG*). We also found a notable population of mucosal-
269 associated invariant T cells (MAIT; *KLRB1, IL18R1*), an unconventional subset recognized for their
270 innate-like effector functions and potential importance in antitumor immunity[33]. In addition to these well-
271 defined T cell subsets, we identified a conserved cluster (ChopT) characterized by the expression of
272 *DDIT3*, which encodes the transcription factor CHOP (Fig. S5A-C). CHOP is a downstream sensor of
273 severe endoplasmic reticulum (ER) stress, and acts as a major negative regulator of both CD8+ and CD4+
274 T cell effector function[34].
275 We next explored how exosome treatment alters native TIL function by performing differential
276 cell proportion analysis (Table S12). We saw 13.6-fold expansion of ChopT cells, coupled with 5.3-fold
277 and 6.5-fold contraction of Tcm and MAIT, respectively, based on immune cell proportions within each
278 treatment group (Fig. 5C). Further, GSEA analysis restricted to immune cells highlighted enhanced anti-
279 inflammatory signaling via interleukin-10 (IL-10) and decreased proinflammatory signaling via the tumor
280 necrosis factor (TNF) superfamily (Fig. 5D, Fig. S5D, Table S13)[30]. We also identified 1.5-fold and 1.8-
281 fold upregulation of gene sets related to hypoxia and defective metabolism, respectively. Additionally,

282 GSEA revealed upregulation of cytotoxic and effector responses, including antigen binding and T cell
283 receptor (TCR) signaling, in ND*exo*-PDOs (Fig. 5d). Collectively, these data demonstrate a clear and
284 distinct profile of immune evasion in T2D*exo* compared to ND*exo*-PDOs.

285 To further investigate the emergence of ER-stressed T cells in T2Dexo-PDOs, we performed
286 pseudotime analysis on the T cell compartment (Fig. 6A). This approach allowed us to map activation and
287 differentiation trajectories of TILs under the influence of T2D-derived exosomes. In NDexo-PDOs, $CD8^+$
288 T cells followed canonical activation and differentiation pathways toward effector and memory states. In
289 contrast, $CD8^+$ T cells in T2Dexo-PDOs deviated sharply from this trajectory, branching instead into an
290 alternative path marked by ER stress, metabolic dysfunction, and effector failure (Fig. 6B). This
291 dysfunctional path was enriched for genes involved in the unfolded protein response (UPR), oxidative
292 stress, and apoptosis — including high expression of *DDIT3* and *XBP1* — and was depleted for key
293 regulators of T cell function and persistence, such as *IL7R*, *GZMK*, and *TBX21* (Fig. 6C-E, Table S14).
294 This finding is consistent with other reports of T-bet repression in ER-stressed T cells[34]. We also observed
295 upregulation of *IDO1*, a tryptophan-catabolizing immunoregulatory gene, further supporting the
296 emergence of a checkpoint-independent suppressive program. These findings suggest that T2D-derived
297 exosomes redirect T cell differentiation away from effector fates, instead driving a chronic dysfunction
298 program underpinned by ER stress, metabolic reprogramming, and transcriptional suppression.

299 To independently validate these findings in a broader clinical context, we applied this ChopT
300 signature to our recently assembled pan-breast cancer single-cell atlas[21]. We calculated per-cell
301 enrichment scores for the ChopT program, along with canonical and curated T cell modules representing
302 effector function, cytotoxicity, IFN-γ signaling, and stress-related pathways. Across this large and diverse
303 clinical cohort, we observed that ChopT-high cells consistently exhibited features of stress-induced
304 dysfunction (Fig. S5E). Specifically, ChopT module scores showed positive correlations with stress-
305 related circuits (e.g., $\rho = 0.34$ for hypoxia score; $\rho = 0.30$ for UPR score; $\rho = 0.24$ for ER stress apoptosis
306 score; $p < 1e{-}10$), and negative correlations with key effector-related programs (e.g., $\rho = -0.24$ for effector
307 score, $\rho = -0.14$ for cytotoxicity score, $\rho = -0.12$ for interferon-γ signaling; $p < 1e{-}10$). These results

308 confirm that the ChopT transcriptional program marks a reproducible, functionally impaired T cell state
309 enriched for ER stress signatures, validating the PDO-derived observations in primary human tumors.
310 They further support the interpretation that ER stress is a central driver of T cell dysfunction in T2D-
311 influenced TMEs, potentially overriding classical checkpoint-based mechanisms.
312

313 **Exosomes modulate intercellular communication in T2D*exo*-PDOs**

314 To further characterize the immune evasive TME of T2D*exo*-PDOs compared to ND*exo*-PDOs, we
315 performed ligand-receptor interaction analysis[35] between all identified cell types (Fig. 7A-D, Fig. S6A-
316 B). Overall, 95 pathways relating to 1142 genes were involved in building the communication network,
317 including 69 conserved pathways, 10 ND*exo*-specific and 16 T2D*exo*-specific pathways (Fig. 7E, Fig.
318 S6C-D, Table S14). Here, we focused our analysis on a subset of biologically relevant pathways associated
319 with immune regulation and tumor-promoting signaling. This analysis revealed upregulated NOTCH (e.g.,
320 JAG1 - NOTCH1) and bone morphogenic protein (BMP; e.g., BMP7 - [BMPR1B+BMPR2]) signaling in
321 T2D*exo*-PDOs, promoting stem-like characteristics and resistance to apoptosis[36]. These findings are
322 supported by our previous work, where we consistently observed downregulation of apoptosis in T2D
323 exosome-treated models[8,24]. Additionally, T2D*exo*-PDOs exhibited enhanced extracellular matrix
324 remodeling with heightened interactions involving MMPs (e.g., MMP2 - ([TGAV+ITGB3]) crucial for
325 tumor cell invasion and migration[37]. Further, T2D*exo*-PDOs showed increased TNF-related apoptosis-
326 inducing ligand (TRAIL) signaling (e.g., TNFSF10 - TNFRSF10B), which has been linked to
327 immunosuppression within the TME[38]. Conversely, ND*exo*-PDOs displayed upregulated communication
328 involving MHC class-I, MHC class-II, and CXCL signaling, indicative of a more robust antitumor
329 immune response[30]. All changes we report were statistically significant.

330 We observed a dense communication network in T2D*exo*-PDOs among basal-like tumor cells and
331 CAFs with all other annotated cell types (Fig. 7F). Focusing specifically on differential T cell ligand-
332 receptor interactions, T2D*exo*-PDOs demonstrated distinct signaling alterations, notably in the
333 thrombospondin pathway (Fig. 7G, Fig. S7A-B). This pathway is known for its immunosuppressive action

334 in T cells, promoting tumor escape mechanisms in breast cancer[39]. Notably, we have previously identified
335 TSP5, a member of the thrombospondin family, as significantly enriched in T2D-derived exosomes
336 compared to those from ND[8]. In contrast, ND*exo*-PDOs exhibited specific activity in the CypA pathway,
337 which is known to significantly limit tumor growth and enhance antitumor immunity[40]. This ligand-
338 receptor analysis further substantiates the role of T2D-derived exosomes in fostering a more aggressive
339 and immune-suppressed TME.
340

341 ## Discussion

342 T2D has long been established as a risk factor for poorer prognosis of breast cancer across
343 numerous population studies[1]. Epidemiological data indicate that women with T2D have a higher
344 incidence of breast cancer compared to ND and they often present with more aggressive tumor
345 phenotypes[27]. Meta-analyses and large-cohort studies have reinforced these findings, suggesting that
346 metabolic dysregulation in T2D may contribute to the pathogenesis and progression of breast cancer[41].
347 Much of the existing research has focused on tumor-intrinsic properties, including insulin-like growth
348 factor signaling and excess glucose availability feeding tumor growth[1]. However, the role of the TME in
349 this comorbidity has been largely overlooked. In this study, we aimed to investigate the impact of
350 metabolic dysregulation in T2D on breast cancer aggressiveness and TME dynamics.

351 Exosomes have emerged as critical mediators of intercellular communication, enhancing cancer
352 progression across various tumor types[5]. Of particular interest, plasma-derived exosomes from individuals
353 with T2D have been shown to induce upregulation of gene sets associated with EMT, invasion, metastasis,
354 and CSC formation in cancer cell lines[8,9]. Despite their significant influence on recipient cell behavior, it
355 remains unclear how T2D-derived exosomes may alter niche dynamics within the TME. In this study, we
356 extended our previous findings by utilizing PDOs to investigate exosomal signaling within the breast
357 TME. By examining these communication networks, we sought to elucidate how exosomes contribute to
358 breast cancer aggressiveness in the context of T2D. We used plasma-derived exosomes to simulate the
359 influence of T2D-associated systemic factors on the TME. Although this approach does not entirely

capture the complexity of PDOs from T2D samples, it provided a robust platform for exploring how T2D-derived exosomes contribute to a more aggressive and immunosuppressive TME.

Here, we describe a novel breast cancer PDO methodology that facilitates *in vitro* TME study by uniquely preserving native TILs and stroma. Whereas previous researchers have generated organoids that include primary TILs[42], these methods have not been established for breast cancer. Our approach, characterized by a short-term culture, offers advantages for experimental throughput and timely data acquisition that accelerates the pace of research and potential therapeutic development. By preserving native TIL populations, our model system allows for accurate modeling of human tumor-immune interactions, as opposed to traditional epithelial-only organoid models[43,44], or models that rely on the co-culture reconstitution of peripheral blood [45]. Importantly, our method maintains a diverse array of endogenous immune cell types, including B cells and macrophages, alongside T cells, unlike reconstitution models that use clonally expanded or TCR-engineered populations[46].

In this study, we found that T2D*exo*-PDOs displayed enhanced EMT and CSC characteristics compared to ND*exo*-PDOs. Specifically, we observed upregulation of multiple gene sets related to these pathways, including NOTCH signaling, WNT signaling, EMT, migration, and multi-cancer invasiveness signatures (Fig. 2A,C-D). Furthermore, projecting the T2D*exo*-induced gene signature onto the TCGA and METABRIC datasets revealed a strong association with poor patient survival outcomes (Fig. 2G). Pseudotime analysis revealed distinct modules of co-regulated gene expression, with Module 5 marked by EMT genes (Fig. 4D). Ligand-receptor analysis further highlighted the influence of NOTCH signaling on intercellular communication in T2D*exo*-PDOs (Fig. 7E). Morphological assessments supported these findings, as T2D*exo*-PDOs displayed pronounced budding (Fig. 2E-F). The networks that we see perturbed are remarkably similar to what we have already published in multiple T2D exosome models including breast cancer cell lines[8,9,24], suggesting a conserved mechanism of action of exosomes. These findings underscore the profound impact of metabolic dysregulation on breast cancer progression, highlighting the need for targeted therapeutic strategies that address the altered niche dynamics induced by T2D-derived exosomes.

386 In contrast, we observed suppression of immune function in T2D*exo*-PDOs compared to ND*exo*-
387 PDOs, characterized by downregulation of gene sets involved in multiple steps of immune function,
388 including cytotoxic signaling, activation, cytokine production, and proliferation (Fig. 2A,C). Restricting
389 our analyses to the immune compartment, we further observed upregulation of IL-10 signaling and
390 hypoxia signatures, alongside downregulation of immune activation and effector function programs in
391 T2D*exo*-PDOs (Fig. 5D). A deeper analysis of the immune state dynamics revealed expansion of ChopT
392 cells (Fig. 5A, Fig. S5A-C), a distinct and conserved T cell state indicative of severe ER stress. Critically,
393 these cells emerged along a divergent pseudotime trajectory (Fig. 6A), bypassing canonical effector and
394 memory differentiation pathways in favor of a transcriptional program marked by metabolic dysfunction,
395 UPR activation, and loss of effector capacity. This reprogramming highlights a checkpoint-independent
396 mechanism of T cell suppression, wherein ER stress fundamentally redirects differentiation toward a
397 dysfunctional state.

398 Interestingly, our ligand-receptor analysis highlighted T2D*exo*-specific TRAIL signaling (Fig.
399 7E), which has been linked to the UPR[38]. Notably, thrombospondin signaling was also specifically active
400 in T2D*exo*-T cells (Fig. 7G), aligning with our previous findings of TSP5 upregulation in T2D-derived
401 exosomes compared to ND controls[8]. This finding highlights the significant role of thrombospondin
402 family proteins in exosome effector function, influencing not only tumor cells but also the broader TME.
403 Interestingly, we did not observe a significant change in Teff proportions, contrary to what might be
404 expected in the pro-tumorigenic TME in T2D; instead, there was contraction of MAIT cells (Fig. 5C),
405 consistent with reports of diminished MAIT frequency and functionality in adults with T2D, particularly
406 in obese patients[47]. Collectively, these results suggest a coordinated pattern of immune evasion in T2D,
407 driven by ER stress and altered cytokine signaling, likely shaped by the hypoxic and metabolically
408 compromised conditions of the TME.

409 Contrary to our expectations, we did not observe upregulation of checkpoint ligands on T cells,
410 which would have indicated classical exhaustion. Immune exhaustion is a well-characterized mechanism
411 of dysfunction in cancer, marked by sustained expression of inhibitory receptors and progressive loss of

412 effector function[4]. While exhaustion phenotypes are known to worsen in T2D and contribute to poor
413 clinical outcomes[3], the immune profile observed here suggests a distinct, non-canonical pattern of T cell
414 impairment.

415 Our data instead point to ER stress as a central driver of T cell dysfunction. CHOP (*DDIT3*), a
416 downstream effector of the PERK–ATF4 axis of the unfolded protein response (UPR), has been shown to
417 suppress $CD8^+$ T cell function in solid tumors independently of checkpoint signaling[48,49]. The IRE1α–
418 XBP1 branch of the UPR is similarly implicated in regulating hypoxia-related gene expression[50] and
419 inhibiting T cell infiltration and IFNγ production[51], while PERK–eIF2α signaling can directly impair T
420 cell functionality and reduce tumor infiltration[52]. CHOP expression, in particular, has been consistently
421 associated with immunosuppressive signaling and poor T cell effector function[34,53].

422 Given that T2D-derived exosomes robustly activate UPR pathways—as evidenced by elevated
423 *DDIT3* and *XBP1* expression—they may drive T cells into a dysfunctional state prior to the onset of
424 classical exhaustion. Notably, pharmacologic or genetic inhibition of CHOP has been shown to
425 reinvigorate T cell activity [34], highlighting ER stress not only as a biomarker but as a potential barrier to
426 effective immunity.

427 ER stress is also a key pathological mechanism of T2D, contributing to β-cell failure, insulin
428 resistance, and chronic inflammation[54–57]. Our findings are among the first to mechanistically link ER-
429 stressed T cells to the diabetes-associated TME, offering a new perspective on how comorbid metabolic
430 disease reshapes antitumor immunity.

431 These results have direct therapeutic implications. Standard immunotherapies that rely on
432 checkpoint inhibition may be ineffective in this context, where T cells are not classically exhausted but
433 rather reprogrammed by ER stress. This result is consistent with existing literature reporting a diminished
434 response to immunotherapy in T2D cancer patients[58,59]. Given the distinct immune landscape in breast
435 cancer with comorbid T2D, therapeutic strategies must address the specific immunometabolic
436 perturbations observed. Approaches that alleviate ER stress, modulate hypoxic responses, and restore T
437 cell function may hold greater promise than checkpoint inhibitors alone.

438 Our research primarily focused on estrogen receptor-positive tumors, providing valuable insights
439 into the breast cancer TME in the context of T2D. However, we recognize the importance of extending
440 these findings to other breast cancer subtypes, particularly estrogen receptor-negative and triple negative
441 breast cancers, which are more prevalent in individuals with T2D[27]. We are actively expanding our studies
442 to include these subtypes with the aim of broadening the applicability of our findings and providing a
443 more comprehensive understanding of the TME across diverse breast cancer populations. Additionally,
444 while our current study did not investigate how patient metabolic medications might influence exosome
445 payloads, future studies will explore this important aspect. Understanding the impact of factors such as
446 diet, exercise, and weight loss medications on exosome-mediated signaling could uncover potential anti-
447 metastatic and anti-immune evasive benefits mediated by specific miRNAs.

448 Together, these findings enhance our understanding of dynamic interactions within the TME and
449 offer new insights into the significance of novel exosomal communication on tumor biology. Our results
450 suggest that metabolic status, particularly T2D, could be considered in the clinical management of
451 estrogen receptor-positive breast cancer to improve therapeutic outcomes. Given the unique vulnerabilities
452 of this population, we strongly advocate for the initiation of targeted clinical trials to explore the TME in
453 these 120 million underserved and understudied patients. Addressing these gaps in knowledge and care
454 could pave the way for more effective, personalized treatment strategies, ultimately improving survival
455 and quality of life for this high-risk group.

456

457 ## Materials and Methods

458 **Patient sample collection**

459 This study was conducted with approval from the Boston University (BU) Institutional Review
460 Board (IRB), ensuring adherence to ethical standards. Informed consent was obtained from each
461 participant prior to enrollment. Breast tumor tissues were harvested from three patients with histologically
462 confirmed estrogen receptor-positive breast cancer during resection surgery. None of the patients had
463 received chemotherapy or radiotherapy prior to surgery, avoiding potential confounders in tumor biology.

464 The collected tissues were processed immediately after resection. Samples were aseptically minced into
465 approximately 1mm^3 chunks using sterile scalpel blades, facilitating even freezing and subsequent
466 thawing. Chunks were then cryopreserved in Cryostor® CS10 freezing media (StemCell, #100-1061),
467 designed to minimize cryoinjury, at a controlled cooling rate of -1°C per minute, and stored at -196°C
468 until further processing.
469
470 **Tissue digestion and organoid generation**
471 PDOs were cultured from cryopreserved breast tumor samples following a modified version of
472 previously published protocols[11,43,44]. A two-step enzymatic digestion process was implemented to ensure
473 gentle dissociation while preserving vital stromal and immune subsets. Initially, tissues were incubated at
474 37°C for 1 hr under 200 rpm with 2 mg/mL collagenase III (StemCell, #07422) in a complete medium
475 consisting of Hyclone DMEM/F/12 1:1 (Thermo Scientific, #SH30023.01) supplemented with 15mM
476 HEPES, 2.5mM L-glutamine, 10 µg/mL gentamicin (Sigma, #G1272), 1% penicillin/streptomycin
477 (Sigma, #516106), 2.5 µg/mL Amphotericin B (Fisher, #MT30003CF), 5mM nicotinamide (Sigma,
478 #N0636), 1.25 mM N-acetylcysteine (Sigma, #A9165), 1x B27 supplement (Fisher, 17-504-044), 250
479 ng/mL R-spondin 3 (Sigma, #SRP3323), 5 nM heregulin (StemCell, #78071), 5ng/mL KGF (StemCell,
480 #78046), 20 ng/mL FGF10 (StemCell, #78037), 5ng/mL EGF (StemCell, #78006), 100 ng/mL Noggin
481 (StemCell, #78060), 500 nM A83-01 (StemCell, #72022), 5 µM Y-27632 (Fisher, #72302), and 500 nM
482 SB202190 (Sigma, #S7067). After this initial digestion, the supernatant containing small cell clusters was
483 carefully removed. Fresh digestion medium was then added to the remaining larger tissue chunks for an
484 additional hour to complete the dissociation process. Following digestion, tissue chunks were washed with
485 DMEM/F12 and passed through a pre-wetted 100 µm filter to remove any undigested fragments and
486 debris. The flow-through was then pelleted and resuspended in Geltrex® (Thermo, #A1413201) BME at
487 4°C then seeded to form domes in pre-warmed 24-well plates. Plates were inverted and allowed to
488 polymerize at 37°C for 30 min. Subsequently, 500 µL of pre-warmed complete medium was gently added
489 per 35 µL BME dome to maintain the PDOs. After initial seeding, PDOs were cultured for only 3 days

prior to any downstream treatments in order to maintain native TIL populations, ensuring their viability and functionality for subsequent analyses.

Exosome isolation and characterization

Patient whole blood was collected from noncancerous individuals at the Boston Medical Center Diabetes Clinic following IRB-approved protocols and with informed consent. The blood samples, one from a diabetic donor (HbA1c 9.3%) and one from a ND donor, were used exclusively for exosome isolation and were not associated with the individuals from whom breast tumor tissues were obtained for PDO generation. Blood samples were centrifuged at 16,000 rpm at 4°C for 30 min to separate plasma, which was then further clarified by additional centrifugation and filtration through a 0.2 μm filter to remove large vesicles or apoptotic bodies. Plasma was prepared to be platelet free and isolated within 30 minutes of the blood collection. Exosomes were isolated using size exclusion chromatography with qEV columns (IZON, product code 1CS-35; RRID:SCR_025764) equipped with spherical beads featuring 35 nm pore sizes, fractionating exosomes ranging from 35 nm to 150 nm in diameter. To minimize experimental variability and focus on the most informative metabolic contrasts, we selected exosome donors through a targeted screening process. The T2D donor, a postmenopausal female selected to mitigate potential estrogen-related effects on exosomal cargo[60–62], was chosen based on having the highest HbA1c level among those not on metabolic drugs, including metformin. The ND donor selected was not taking any medications. Preliminary screening indicated that exosomes from this T2D patient produced the most pronounced differences between the treatment group and negative control. Importantly, previous work has demonstrated that ND exosomes elicit consistent biological effects across donors[9], reducing concerns about variability in the ND condition. Purified exosomes were eluted in DMEM/F12 and stored at 4°C. Storage of the isolated exosomes was short term (<24 hours post isolation). Size distribution and concentration of exosomes were measured using a NanoSight NS300 system (Malvern Panalytical). Quality control for the exosomal preparations was performed according to previously published protocols[8,9].

516

517 **Exosome treatment**

518 We estimated the number of cells within each PDO sample to normalize exosome treatments.
519 Traditional cell counting methods were not suitable as they would disrupt the architecture of the PDOs;
520 instead, we calculated the total cell number by assuming the PDOs were spherical and determining their
521 volume. This volume was then divided by the average volume of a single cell to estimate the number of
522 cells per PDO. This estimation process was repeated across multiple PDOs to determine an average cell
523 count per PDO, which was then multiplied by the total number of PDOs to obtain the overall cell count
524 for each sample. PDOs were retrieved from BME domes by liquefying the BME at 4°C for 15 min,
525 followed by centrifugation at 500 rcf for 5 min. Exosomes were isolated from plasma samples of ND and
526 T2D donors, yielding approximately 4.55×10^{11} and 6.57×10^{11} exosomes per milliliter of plasma,
527 respectively. Exosome recovery was consistent between patient groups. For experimental consistency,
528 exosomes were normalized to a concentration of 5,000 particles per PDO cell. PDOs were subsequently
529 seeded to form BME domes into 35mm glass-bottom FluoroDish® plates (World Precision Instruments)
530 as described above. After polymerization, 2mL of pre-warmed complete medium, supplemented with the
531 same concentration of exosomes, was gently added to each BME dome to sustain PDO cultures. PDOs
532 were cultured for an additional 3 days to allow for effective exosome uptake and interaction before
533 proceeding to downstream applications.

534

535 **Microscopy and imaging of organoids**

536 Morphological assessments of PDOs were conducted via reflectance confocal microscopy using
537 Live-Duo LSM 710 system (Zeiss, Thornwood NY; RRID:SCR_018063) at the BU Microscopy Core,
538 equipped with a Plan-Apochromat 20X/0.8 objective (Carl Zeiss Microscopy GmbH) and 543 nm solid
539 state laser. PDOs were mounted directly onto FluoroDish® glass-bottom dishes, leveraging the natural
540 refractive properties of the tissues to negate the need for staining. Images were captured at a resolution of
541 1024x1024 pixels to ensure detailed visualization. Image acquisition was performed at 37°C in a

542 humidified atmosphere containing 5% CO_2, optimal for live-cell imaging. Post-acquisition, images were
543 processed using FIJI software (RRID:SCR_002285)[63]; briefly, brightness and contrast were adjusted
544 before applying automatic thresholding. Morphological parameters including area, perimeter, and
545 circularity of PDOs were calculated via particle analysis. Single cells were excluded by applying size
546 filters greater than 300 μm2.
547

548 **Single-cell library preparation and sequencing**

549 PDOs were enzymatically digested into single cells using TrypLE Express (Thermo Fisher
550 Scientific) to ensure a gentle yet effective separation. Cells were resuspended in 0.1% BSA in PBS and
551 passed through a 40 μm cell strainer to achieve a uniform single-cell suspension. Cells were stained with
552 DAPI to identify and exclude non-viable cells and isolated using a FACSAria II cell sorter (BD
553 Biosciences; RRID:SCR_018934) in the BU Flow Cytometry Core. Sorted cells from each treatment
554 group were loaded into individual wells of a 10X Chromium microfluidics chip for single-cell barcoding.
555 Libraries were prepared using the Chromium Single Cell 3' Library & Gel Bead Kit v3.1 (10X Genomics;
556 RRID:SCR_024537) according to standard protocols. Quality and quantity of the amplified cDNA were
557 assessed using an Angilent Bioanalyzer 2100 High Sensitivity Kit. Libraries were then multiplexed and
558 sequenced on an Illumina NextSeq 2000 platform (RRID:SCR_023614), aiming for a depth of
559 approximately 30,000 reads per cell, which provides sufficient coverage to detect most expressed genes.
560

561 **Single-cell data processing, clustering annotation, and integration**

562 Transcriptomic data were mapped to the human reference genome (GRCh38.p14;
563 RRID:SCR_006553) and assigned to individual cells of origin according to cell-specific barcodes using
564 the Cell Ranger pipeline version 6.0.1 (10X Genomics; RRID:SCR_017344). Filtering, feature selection,
565 clustering, and other secondary analyses were performed using Seurat v5.0.1 (RRID:SCR_016341)[64].
566 Initial preprocessing included the removal of doublets using the DoubletFinder v2.0.4 pipeline
567 (RRID:SCR_018771)[65]. The data were further filtered to exclude cells with high mitochondrial gene

568 expression (>20%) and aberrant unique feature counts (<100, >9000), followed by normalization and
569 identification of highly variable features using scTransform v0.4.1 (RRID:SCR_022146)[65].
570 Dimensionality reduction was carried out via PCA using 50 dimensions, followed by clustering using the
571 graph-based Louvain method with a resolution of 0.5 to identify distinct cellular populations. Cell types
572 within these clusters were then automatically annotated using the SingleR pipeline
573 (RRID:SCR_023120)[17], referencing an established comprehensive single cell atlas of breast cancer patient
574 samples[18]. To harmonize the data across patients and mitigate batch effects, we performed dataset
575 integration using scVI[14] . This methodology was selected over alternatives based on *k*-nearest-neighbor
576 batch effect test, integration local inverse Simpson's index, average silhouette width, and principal
577 component regression comparison from single cell integration benchmarking (scIB) analysis [66].
578

579 **Identification of neoplastic from normal breast epithelial cells**

580 The integrity of tumor cells within clusters was confirmed by performing inferCNV analysis
581 (RRID:SCR_021140)[67], which identified loss of heterozygosity and copy number alterations
582 characteristic of tumor cells compared to normal immune cells present within PDOs. Epithelial cells were
583 classified into normal or neoplastic categories using a method previously described[18]. Briefly, the mean
584 of squared, scaled inferred changes at each genomic locus was used to calculate a genomic instability
585 score for each cell. For each patient, the top 5% of cells with the highest genomic instability scores were
586 used to generate an average CNV profile. Cells were then correlated with this profile to obtain malignancy
587 scores and plotted accordingly.

588 Partitioning around medoids clustering was performed using the pamk function in the fpc v2.2.12
589 package to determine the optimal number of clusters based on silhouette scores. To call normal from tumor
590 cells, a comprehensive grid search over a range of standard deviation multipliers was conducted and
591 applied to both genomic instability and malignancy scores to maximize the average silhouette width. The
592 resulting thresholds were confirmed through visual inspection of scatter plots and histograms of genomic
593 instability and malignancy scores with thresholds clearly demarcated. Thresholds were further validated

594 by comparing expression profiles with cancer-associated genes and pathways including the COSMIC
595 CGC (RRID:SCR_002260)[15] and GOBP_MAMMARY_EPITHELIAL_ PROLIFERATION
596 (RRID:SCR_002143)[16].
597
598 **Differential gene expression and pathway enrichment**
599 Considering that data integration is performed only in the latent space leaving the raw expression
600 profiles untouched, differential expression analysis needs to account for both biological variance and
601 unwanted covariates such as batch effects. To model these technical effects, we performed differential
602 expression analysis using the FindMarkers function in Seurat, using the statistical framework introduced
603 by MAST (RRID:SCR_016340)[68] and setting a latent variable of patient batch. To further explore the
604 biological processes and pathways associated with the differentially expressed genes, we performed
605 functional enrichment analysis using the DAVID Knowledgebase v2024q2 (RRID:SCR_001881)[31].
606 GSEA was also conducted using the FGSEA v1.26.0 package (RRID:SCR_020938), drawing on gene sets
607 from the Molecular Signatures Database (MSigDB; RRID:SCR_016863)[22]. Enrichment scores were
608 normalized, with permutations set to 50,000 times, using an adjusted p-value cut off of 0.05 to filter the
609 significant enrichment results. Expression of specific gene sets of interest were determined by first
610 calculating the average expression score per cell using the AddModuleScore in Seurat, then utilizing a
611 linear mixed-effects regression (LMER) model via the lmerTest v3.1.3 package (RRID:SCR_015656)
612 correcting for batch effect.
613
614 **Survival analysis**
615 To assess the broader clinical relevance of our findings, we derived a composite gene signature
616 reflecting the net transcriptional effect of diabetes-associated exosomal signaling. This signature was
617 constructed by combining the top 100 differentially expressed genes upregulated in T2D-exosome–treated
618 PDOs and downregulated in ND-exosome–treated PDOs, capturing genes enriched in the T2D-like
619 immune phenotype. We applied this signature to bulk RNA-seq data from two large cancer cohorts:

620 TCGA[25] and METABRIC[26]. Breast cancer cases were subsetted for our analyses. Signature scores were
621 computed for each tumor sample using the mean expression of signature genes normalized per dataset.
622 We used the brcaSurv v0.0.1 package to assess associations between signature scores and overall survival,
623 adjusting for age, PAM50 intrinsic subtype, proliferation score, and inflammation score. Cox proportional
624 hazards models were fit separately for each cohort, and patients were stratified by signature tertiles for
625 visualization using Kaplan–Meier survival curves.
626

627 **Signature projection and validation**

628 To validate transcriptional programs observed in the PDO model, we applied gene signature scoring
629 to our recently assembled pan-breast cancer single-cell atlas, comprising 621,200 high-quality cells from
630 138 patients across 8 independent studies[21]. Cells were annotated as epithelial, stromal, or immune based
631 on canonical markers and clustering, and we quantified the proportion of each compartment per patient.
632 For downstream analysis, we focused on the immune compartment. Using the AddModuleScore function
633 from Seurat, we projected the ChopT signature (derived from our PDO dataset), canonical T cell effector
634 modules, and stress-related gene sets from MSigDB onto individual immune cells. We then computed
635 Spearman correlations between ChopT and comparator module scores to assess co-enrichment of ER
636 stress signatures and suppression of effector function.
637

638 **Differential cell type proportion analysis**

639 To compare the abundance of different cell types between experimental conditions in our dataset, we
640 utilized a binomial generalized linear model (GLM) framework via the lmerTest v3.1.3 package
641 (RRID:SCR_015656) to model the count of cell types across conditions while controlling for covariates
642 such as patient batch. Differential cell type proportion was then quantified as a log odds ratio, reporting
643 the enrichment or depletion of cell types across conditions, using estimated marginal means obtained from
644 the binomial model via the emmeans v1.10.1 package (RRID:SCR_018734).
645

646 **miRNA target enrichment**

647 To assess enrichment of predicted and validated miRNA targets among genes downregulated in
648 T2Dexo-treated LTs, we used a one-sided Fisher's exact test and hypergeometric test framework. Target
649 genes for miR-374a-5p, miR-93-5p, and let-7b-3p were obtained via the multiMiR v1.24.0 package[69],
650 including both validated and high-confidence predicted interactions. Enrichment was tested relative to all
651 expressed genes in the dataset.

652

653 **Ligand-receptor analysis**

654 Cell-cell communication within and between tumor and microenvironment populations was analyzed
655 via CellChat v2.1.2 (RRID:SCR_021946)[35] with default configurations. This analysis incorporated a
656 curated database of ligand-receptor interactions, providing a statistical framework for inferring lineage-
657 specific interactions. The T2D*exo*-PDO and ND*exo*-PDO data were extracted and formatted into CellChat
658 format. Data processing and visualization were performed with default settings.

659

660 **Pseudotemporal ordering to infer cell trajectories**

661 Diffusion-pseudotime analysis was performed using the Monocle3 v1.3.5 package
662 (RRID:SCR_018685)[29]. Seurat single cell objects containing epithelial cells were converted into a
663 Monocle object using SeuratWrappers v0.3.4 package (RRID:SCR_022555), followed by standard
664 clustering and trajectory inference. The trajectory was rooted in normal LECs to establish the pseudotime
665 ordering. Differential gene expression along the trajectory was assessed using the graph_test function in
666 Monocle3, identifying genes significantly associated with the progression of cell states. Genes were
667 grouped into modules of co-expression via the find_gene_modules function in Monocle3. Module scores
668 were then calculated for each cell using the AddModuleScore function in Seurat.

669 We also performed pseudotime and hierarchical state analysis on the T cell compartment to
670 investigate immune lineage reprogramming. T cells were first subsetted from the unintegrated Seurat
671 object and reclustered. K2Taxonomer v1.0.7[70] was applied to define a hierarchical taxonomy of T cell

672 states using gene set–level expression features. Pathway enrichment analysis via the runGSEmods
673 function was used to annotate major transcriptional programs across branches. To model T cell
674 differentiation trajectories, we applied Monocle 3 to the same subset. Dimensionality reduction and graph
675 learning were performed using standard parameters, and pseudotime ordering was rooted in Tcm cells,
676 reflecting their early differentiation status. These combined analyses allowed us to capture both lineage
677 structure and underlying pathway signatures associated with dysfunctional T cell fates.
678
679 **Statistical analysis**
680 Statistical analyses were performed using R version 4.3.1 (RRID:SCR_001905). Specific tests are
681 indicated in the figure legends along with the statistical significance.
682
683 **Data and code availability**
684 All raw data will be available to download from GEO. Processed data will be available for exploration
685 on CELLxGENE. These will be publicly available at time of publication. Metadata for the different PDOs
686 is available in Supplementary Table S1. All original code will be deposited at
687 https://github.com/montilab/BrCaExoPDO/.
688
689 *Acknowledgments*
690 We are grateful for David Sherr, Robert Fisher, and Jason Weis for their valuable discussions on data
691 interpretation and manuscript revision, Lina Kroehling for her advice on analysis and statistics, Vinay
692 Duggineni and Christina McConney for their help with cell cluster annotation, and Emma Kelley and
693 Ruben Dries for their support during the setup of the PDO platform. We appreciate the technical assistance
694 and expertise of the BU Flow Cytometry Core Facility, Christopher Williams at the BU Single Cell
695 Sequencing Core, Yuriy Alekseyev at the BU Microarray Sequencing Core, and Michael Kirber at the
696 BU Cellular Imaging Core. We also thank the study nurses and clinical staff that obtained samples and
697 the patients who generously consented for the research use of these samples. Finally, we appreciate

698 members of the Denis and Monti laboratories as well as students and faculty in the BU Virology,
699 Immunology, and Microbiology Department and Immunology Training Program for their feedback and
700 support.
701

702 *Author contributions*

703 Conception and design: C.S.E., G.V.D. Methodology: C.S.E., S.M., G.V.D. Acquisition of data: C.S.E.
704 M.S., H.K., A.I., K.M., N.K. Analysis and interpretation of data: C.S.E., A.C., S.M. Writing, editing, and
705 revision of manuscript: C.S.E., M.S., A.C., G.V.D. Study supervision and funding: G.V.D.
706

707 *Declaration of interests*

708 The authors declare no competing interests.

Figures

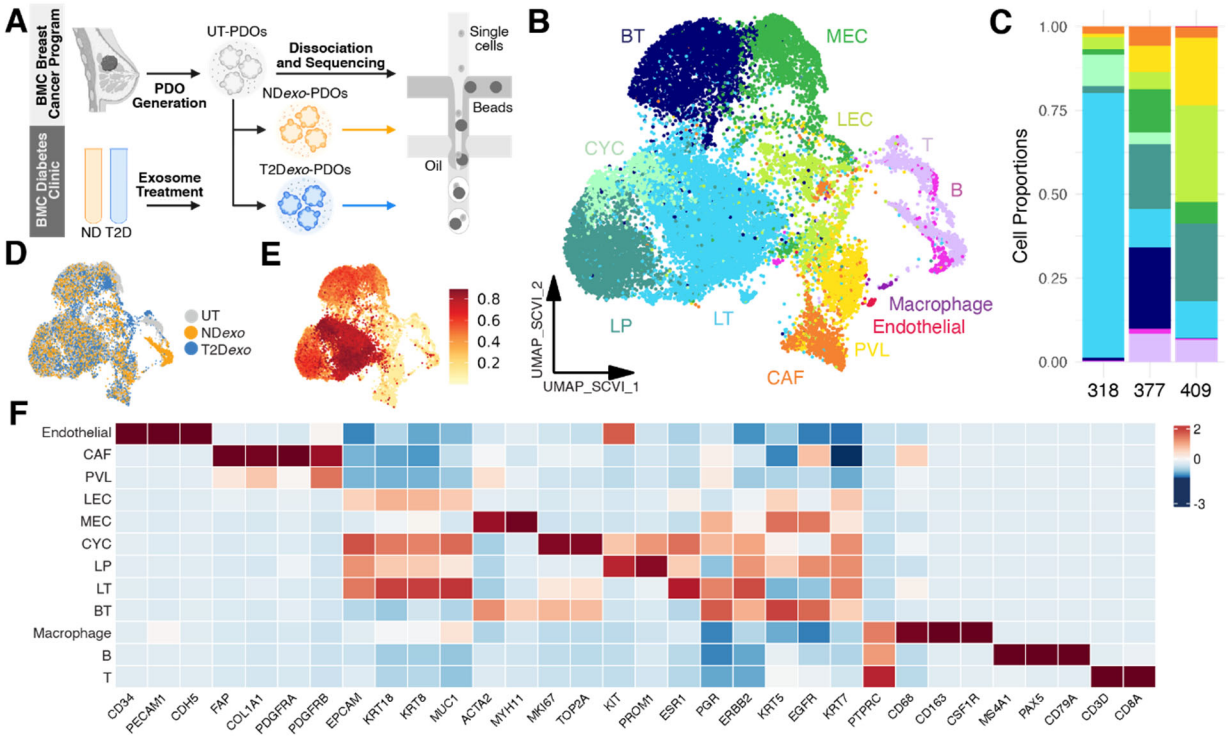

Fig 1: Cellular characterization of PDOs.

A. Illustration of scRNAseq workflow in PDO model of breast cancer TME. **B.** scVI-integrated UMAP visualization of PDOs colored by broad cell type annotation. N = 24,599 from three patients. BT (4,226 cells) denotes basal-like tumor cells; CAF (1,149 cells) denotes cancer-associated fibroblasts; CYC (1,223 cells) denotes cycling epithelial cells; LEC (1,254 cells) denotes normal luminal epithelial cells; LT (7,514 cells) denotes luminal-like tumor cells; MEC (2,382 cells) denotes normal myoepithelial cells; PVL (1,487 cells) denotes perivascular-like cells. **C.** Relative proportion of cell types in each patient highlighting conservation of major lineages. Colors denote the same cell types in A. **D/E.** scVI-integrated UMAP colored by treatment (**D**) and malignancy score as calculated from genomic instability (**E**). **F.** Heatmap showing expression of canonical marker genes per lineage.

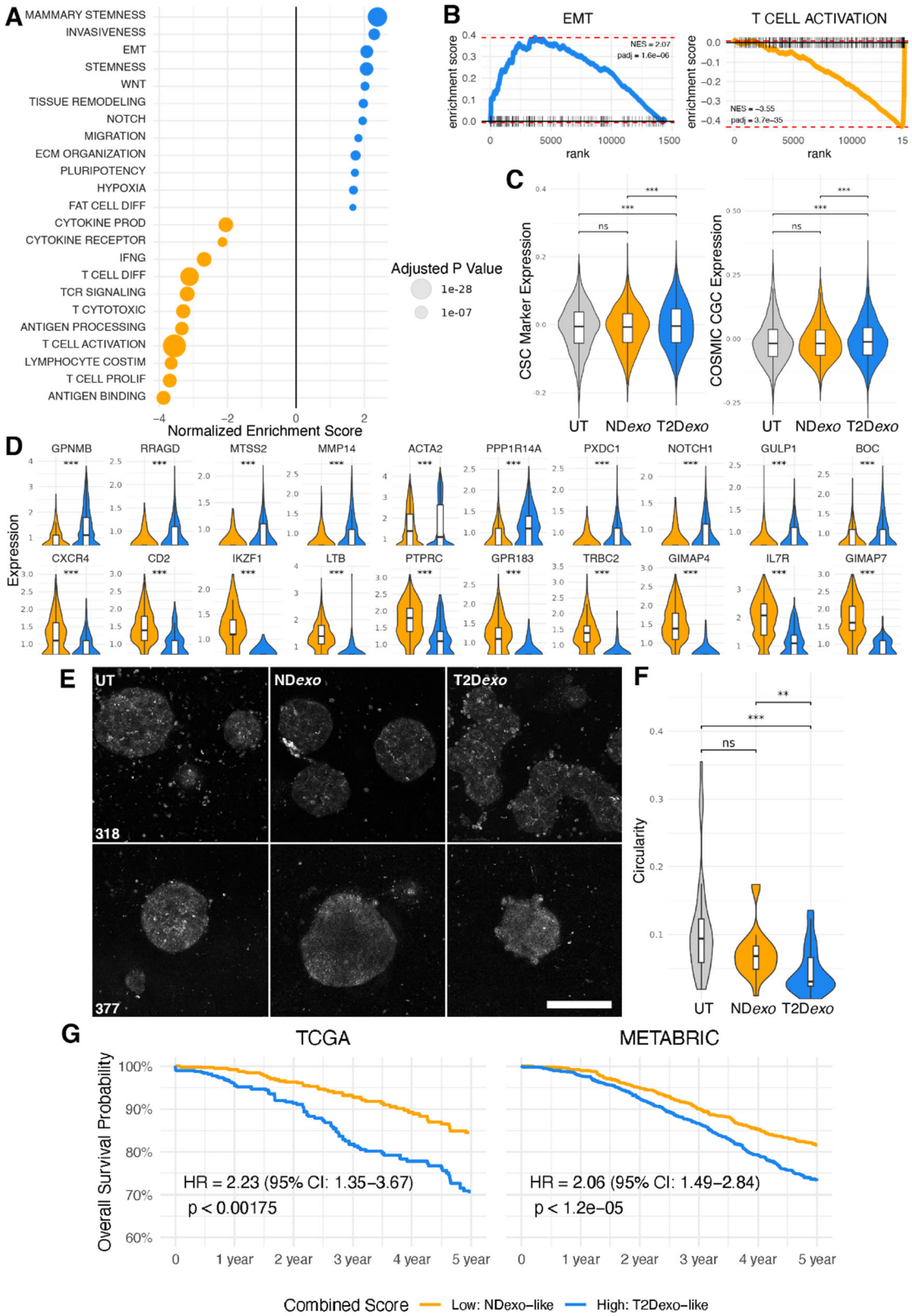

Fig 2: Increased aggression in T2D*exo*-PDOs compared to ND*exo*-PDOs.

A. Bubble plot summarizing statistically significant gene sets enriched in differentially expressed gene sets between T2D*exo*-PDOs (blue) and ND*exo*-PDOs (orange) identified with gene set enrichment

725 analysis (GSEA). Size of dot is scaled to adjusted p value. **B.** GSEA enrichment plots for representative
726 gene sets upregulated (top) and downregulated (bottom) in T2D*exo*-PDOs compared to ND*exo*-PDOs. **C.**
727 Violin plots of COSMIC CGC (left) and canonical CSC gene expression (right). Significance calculated
728 via linear mixed effects model, ***<0.001, **<0.01, *<0.05. **D**. Violin plots of top differentially expressed
729 genes. **E.** Representative confocal images of UT (left), ND*exo* (middle) and T2D*exo* (right) per patient.
730 Scale bar = 100 μm. **F.** Violin plots of calculated circularity of PDOs. Singlets were removed during
731 thresholding. Significance calculated via pairwise Wilcoxon Rank Sums test with Bonferroni correction,
732 ***<0.001, **<0.01, *<0.05. **G.** Projection of composite gene signatures capturing diabetes-associated
733 exosomal effects onto TCGA (left) and METABRIC (right) cohorts. Cox proportional hazards model
734 adjusted for age, proliferation score, inflammation score, and molecular subtype.

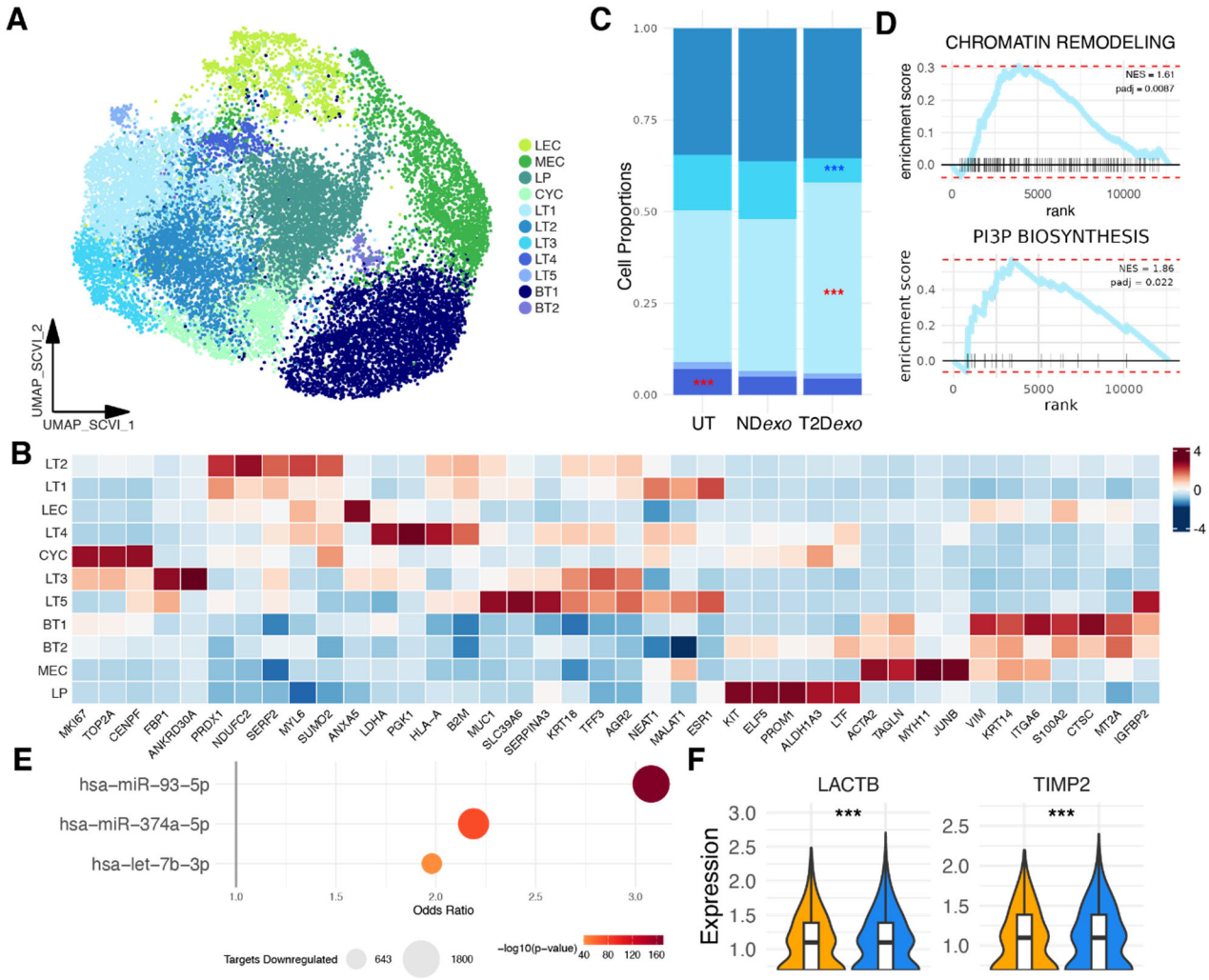

Fig 3: Tumor population dynamics in T2D*exo*-PDOs.

A. UMAP visualization of reclustered scVI-integrated epithelial cells. BT1-2 (n = 4,084; n = 142) denote basal-like tumor subclones; CYC (n = 1,223) denotes cycling epithelial cells; LEC (n = 1,254) denotes normal luminal epithelial cells; LP (n = 3,574) denotes luminal progenitor cells; LT1-5 (n = 3,397; n = 2,669; n = 925; n = 398; n = 125) denote luminal-like tumor subclones; MEC (n = 2,382) denotes normal myoepithelial cells. **B.** Heatmap showing expression of canonical and top differentially expressed marker genes per subclone. **C.** Relative proportion of luminal-like tumor subclones per treatment group. Red (blue) stars indicate significantly expanding (contracting) clusters. Significance calculated via binomial linear regression model, ***<0.001, **<0.01, *<0.05. **D.** GSEA enrichment plots for representative gene sets upregulated in LT1. **E.** Bubble plot summarizing enrichment of predicted and validated targets for individual T2D*exo*-associated miRNAs among downregulated genes in LTs treated with T2D*exo* vs.

747 ND*exo*. Odds ratios from Fisher's exact test are shown for each miRNA; bubble size corresponds to the

748 number of targets downregulated. **F.** Violin plots showing expression of negative regulators of MMPs.

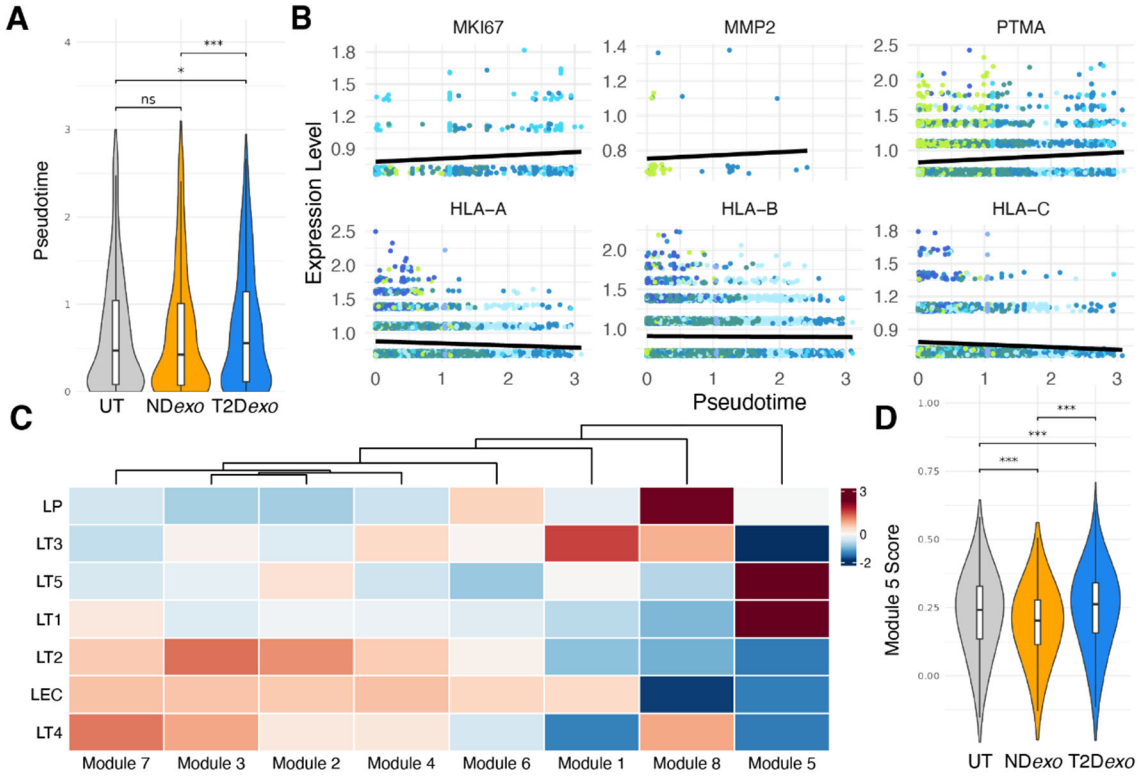

Fig 4. Tumor cell evolution.

A. Violin plots of pseudotime calculated for luminal-like epithelial cells per treatment group. Significance calculated via linear mixed effects model, ***<0.001, **<0.01, *<0.05. **B.** Scatter plots of gene expression as a function of pseudotime. Dot color denotes epithelial cell subtype assigned to cells. Black line showing linear regression of best fit. Genes determined via graph autocorrelation. **C.** Heatmap of gene module expression in epithelial cell subtypes. **D.** Violin plots of expression of Module 5 in luminal-like epithelial cells. Significance calculated via linear mixed effects model, ***<0.001, **<0.01, *<0.05.

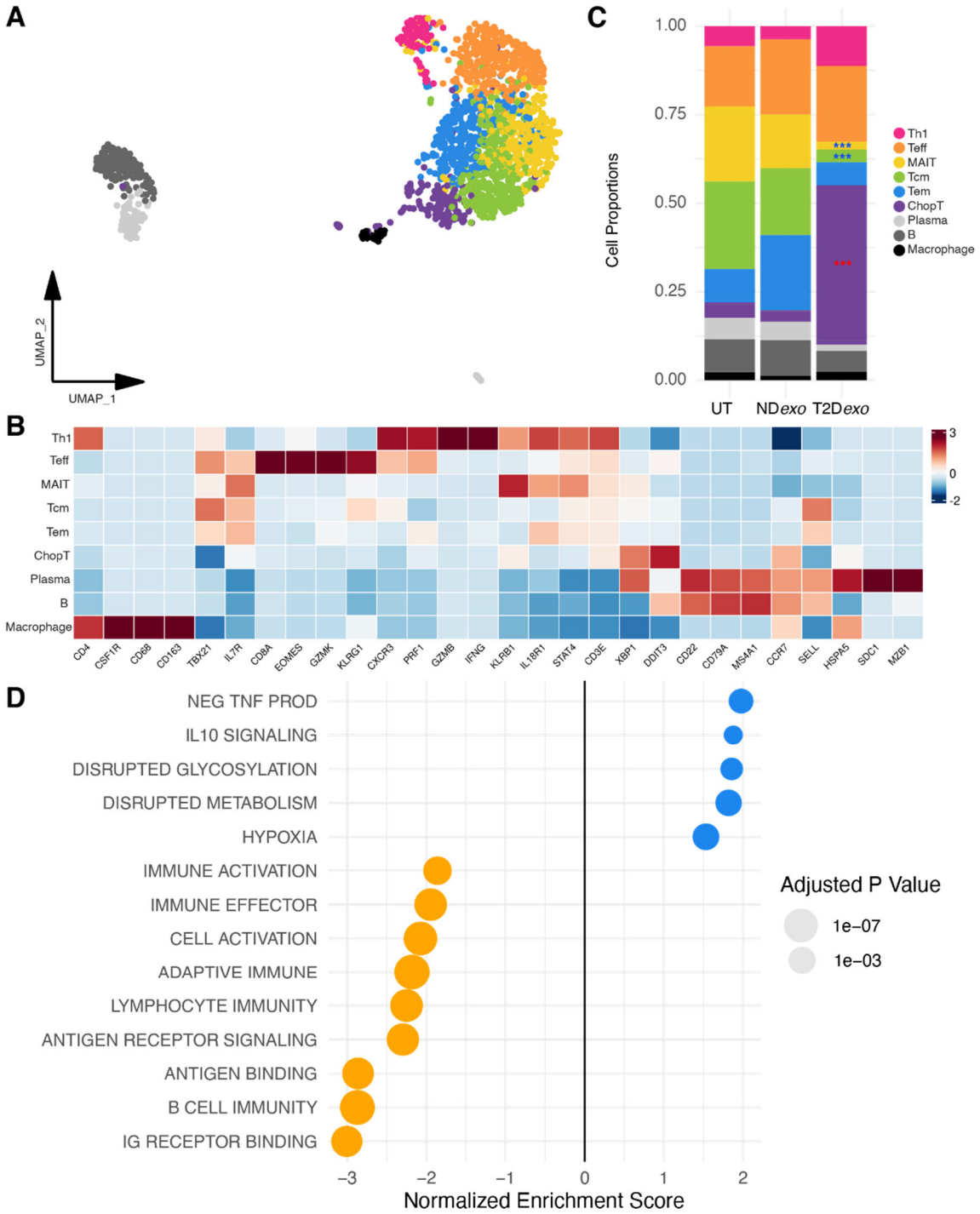

Fig 5: Perturbed immune signaling in T2D*exo*-PDOs.

A. Unintegrated UMAP visualization of clustered immune cells. ChopT (n = 135) denote *DDIT3*+ T cells; MAIT (n = 284) denote mucosal-associated invariant T cells; Tcm (n = 343) denotes central memory T cells; Tem (n = 274) denotes effector memory T cells; Teff (n = 374) denotes effector T cells; Th1 (n = 90) denote T helper 1 cells. **B**. Relative proportion of immune compartment per treatment. Red (blue) stars indicate significantly expanding (contracting) clusters. Significance calculated via binomial linear

764 regression model, ***<0.001, **<0.01, *<0.05. **C.** Heatmap showing expression of canonical marker
765 genes per immune cell state. **D.** Bubble plot summarizing statistically significant gene sets enriched in
766 differentially expressed genes between the immune compartments of T2D*exo*-PDOs (blue) and ND*exo*-
767 PDOs (orange) identified during gene set enrichment analysis (GSEA). Size of dot is scaled to adjusted p
768 value.
769

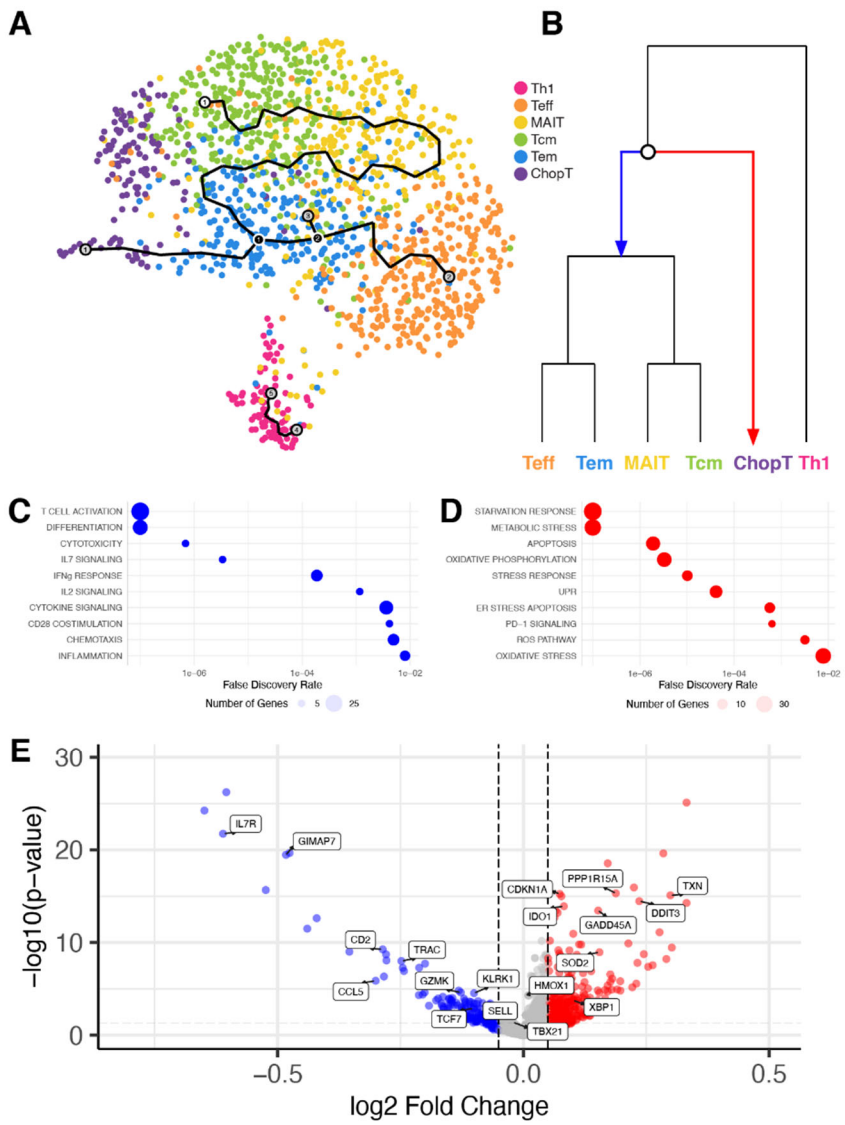

Fig. 6: Pseudotime analysis reveals divergent fates in the T cell compartment.

A. Trajectory inferred from T cells. **B.** Phylogenetic tree showing branch point leading either toward typical development (blue) or toward ChopT phenotype (red). **C/D.** Bubble plot summarizing statistically significant gene sets enriched along the trajectory toward proper development (**C.,** blue) or toward the ChopT phenotype (**D.**, red). Dot size reflects the number of genes detected per gene set. **E.** Volcano plot of top differentially expressed genes at the branch point.

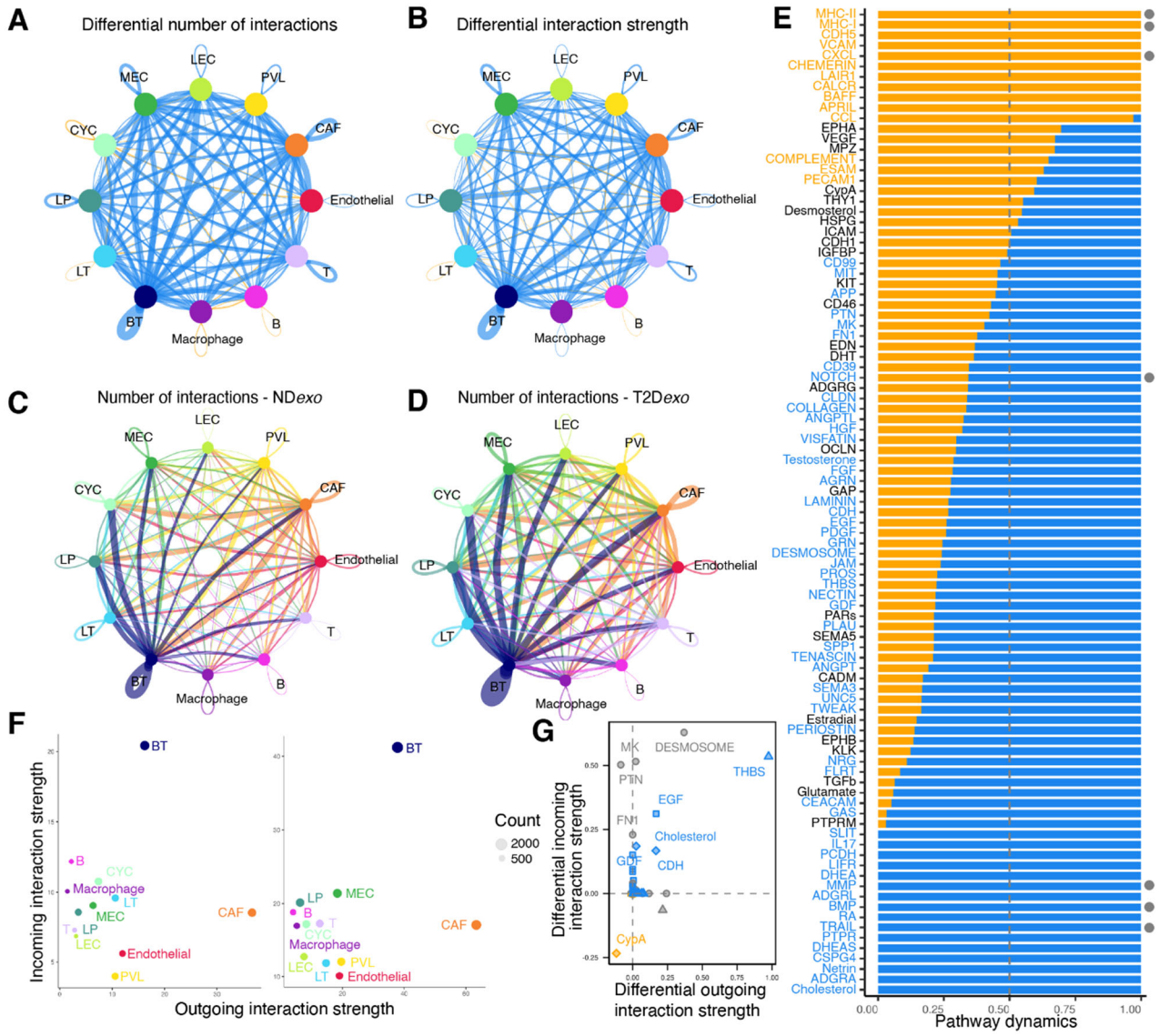

Fig 6. T2D*exo* modulates intercellular communication networks.

A. Circle plot showing the number of interactions among different cell types. The blue (orange) colored edges represent increased (decreased) signaling in T2D*exo* compared to ND*exo*-PDOs. **B**. Circle plot showing the differential interaction strength among different cell types. The blue (orange) colored edges represent increased (decreased) interaction strength in T2D*exo* compared to ND*exo*-PDOs. **C/D.** Circle plot displaying the number of interactions and the strength of interactions between cell types in ND*exo*-PDOs (**C**) and T2D*exo*-PDOs (**D**). The number of lines represents the number of interactions, and the thickness of lines is proportional to the strength of the interactions. **E.** Stacked bar plot showing the overall information flow of each significant signaling pathway ($p < 0.01$). The vertical dashed line indicates the position where the sample accounts for 50% of the overall information flow. Label color is determined by

789 a significantly larger contribution from T2D*exo* (blue) or ND*exo*-PDOs (orange). Pathways equally
790 important in both datasets are labeled in black. *P* value determined by paired Wilcoxon test according to
791 CellChat. Grey dots indicate highlighted pathways highlighted within the main text. **F.** Scatter plot of
792 dominant senders and receivers for ND*exo* (left) and T2D*exo*-PDOs (right). **G.** Scatter plot of the signaling
793 changes associated with T cells in T2D*exo* (blue) or ND*exo*-PDOs (orange). Shared pathways are labeled
794 in gray. Collagen and laminin pathways have been removed from plot for ease of visualization.

References

1. Ennis, C. S., Llevenes, P., Qiu, Y., Dries, R. & Denis, G. V. The crosstalk within the breast tumor microenvironment in type II diabetes: Implications for cancer disparities. *Front Endocrinol* (2022) doi:10.3389/fendo.2022.1044670.

2. Daryabor, G., Atashzar, M. R., Kabelitz, D., Meri, S. & Kalantar, K. The Effects of Type 2 Diabetes Mellitus on Organ Metabolism and the Immune System. *Front Immunol* **11**, 1582 (2020).

3. Nojima, I. *et al.* Dysfunction of CD8 + PD-1 + T cells in type 2 diabetes caused by the impairment of metabolism-immune axis. *Sci Rep-uk* **10**, 14928 (2020).

4. Zhang, Z. et al. T *Cell* Dysfunction and Exhaustion in Cancer. *Frontiers Cell Dev Biology* **8**, 17 (2020).

5. Jafari, N., Llevenes, P. & Denis, G. V. Exosomes as novel biomarkers in metabolic disease and obesity-related cancers. *Nat. Rev. Endocrinol.* **18**, 327–328 (2022).

6. Clement, E. et al. Adipocyte extracellular vesicles carry enzymes and fatty acids that stimulate mitochondrial metabolism and remodeling in tumor cells. *EMBO J.* **39**, e102525 (2020).

7. Lehuédé, C. et al. Adipocytes promote breast cancer resistance to chemotherapy, a process amplified by obesity: role of the major vault protein (MVP). *Breast Cancer Res.* **21**, 7 (2019).

8. Jafari, N. et al. Adipocyte-derived exosomes may promote breast cancer progression in type 2 diabetes. *Sci Signal* **14**, eabj2807 (2021).

9. Jafari, N. et al. Novel plasma exosome biomarkers for prostate cancer progression in co-morbid metabolic disease. *Adv. Cancer Biol. - Metastasis* **6**, 100073 (2022).

10. LeSavage, B. L., Suhar, R. A., Broguiere, N., Lutolf, M. P. & Heilshorn, S. C. Next-generation cancer organoids. *Nat Mater* 1–17 (2021) doi:10.1038/s41563-021-01057-5.

11. Bhatia, S. et al. Patient-Derived Triple-Negative Breast Cancer Organoids Provide Robust Model Systems That Recapitulate Tumor Intrinsic Characteristics. Cancer Res **82**, 1**174**–1192 (2022).

12. Saeki, S. et al. Transcriptomic intratumor heterogeneity of breast cancer patient-derived organoids may reflect the unique biological features of the tumor of origin. Breast Cancer Res **25**, 21 (2023).

821 13. Yuki, K., Cheng, N., Nakano, M. & Kuo, C. J. Organoid Models of Tumor Immunology. *Trends*
822 *Immunol* **41**, 652–664 (2020).
823 14. Gayoso, A. et al. A Python library for probabilistic analysis of single-cell omics data. *Nat.*
824 *Biotechnol.* **40**, 163–166 (2022).
825 15. Sondka, Z. et al. The COSMIC Cancer Gene Census: describing genetic dysfunction across all
826 human cancers. *Nat. Rev. Cancer* **18**, 696–705 (2018).
827 16. Carbon, S. et al. AmiGO: online access to ontology and annotation data. *Bioinformatics* **25**, 288–289
828 (2008).
829 17. Aran, D. et al. Reference-based analysis of lung single-cell sequencing reveals a transitional
830 profibrotic macrophage. *Nat. Immunol.* **20**, 163–**172** (2019).
831 18. Wu, S. Z. et al. A single-cell and spatially resolved atlas of human breast cancers. *Nat Genet* **53**,
832 1334–1347 (20**21**).
833 19. Keren, L. et al. A Structured Tumor-Immune Microenvironment in Triple Negative Breast Cancer
834 Revealed by Multiplexed Ion Beam Imaging. Cell 174, 1373-1387.e19 (2018).
835 20. Soysal, S. D., Tzankov, A. & Muenst, S. E. Role of the Tumor Microenvironment in Breast Cancer.
836 *Pathobiology* **82**, 1**42**–152 (2015).
837 21. Chen, A., Kroehling, L., Ennis, C. S., Denis, G. V. & Monti, S. A highly resolved integrated
838 transcriptomic atlas of human breast cancers. *bioRxiv* 2025.03.13.643025 (2025)
839 doi:10.1101/2025.03.13.643025.
840 22. Subramanian, A. et al. Gene set enrichment analysis: A knowledge-based approach for interpreting
841 genome-wide expression profiles. *Proc. Natl. Acad. Sci.* **102**, 15545–15550 (2005).
842 23. Karolak, A., Poonja, S. & Rejniak, K. A. Morphophenotypic classification of tumor organoids as an
843 indicator of drug exposure and penetration potential. *PLoS Comput. Biol.* **15**, e1007214 (2019).
844 24. Qiu, Y. et al. Insulin Resistance Increases TNBC Aggressiveness and Brain Metastasis via
845 Adipocyte-derived Exosomes. bioRxiv 2024.05.01.592097 (2024) doi:10.1101/2024.05.01.592097.
846 25. Koboldt, D. C. et al. Comprehensive molecular portraits of human breast tumours. *Nature* **490**, 61–

847 70 (2012).
848 26. Curtis, C. et al. The genomic and transcriptomic architecture of 2,000 breast tumours reveals novel
849 subgroups. Nature **486**, 346–352 (2012).
850 27. Palmer, J. R., Castro-Webb, N., Bertrand, K., Bethea, T. N. & Denis, G. V. Type II Diabetes and
851 Incidence of Estrogen Receptor Negative Breast Cancer in African American Women. Cancer Res **77**,
852 6462–6469 (2017).
853 28. Tiainen, S. et al. Tumor microenvironment and breast cancer survival: combined effects of breast fat,
854 M2 macrophages and hyaluronan create a dismal prognosis. *Breast Cancer Res Tr* **179**, 565–575 (2020).
855 29. Cao, J. et al. The single-cell transcriptional landscape of mammalian organogenesis. Nature **566**,
856 496–502 (2019).
857 30. Gerashchenko, T. et al. Breast Cancer Immune Landscape: Interplay Between Systemic and Local
858 Immunity. *Adv. Biol.* **8**, e2400140 (2024).
859 31. Sherman, B. T. et al. DAVID: a web server for functional enrichment analysis and functional
860 annotation of gene lists (2021 update). *Nucleic Acids Res.* **50**, W216–W221 (2022).
861 32. Gahete, M. D. et al. Changes in Splicing Machinery Components Influence, Precede, and Early
862 Predict the Development of Type 2 Diabetes: From the CORDIOPREV Study. *EBioMedicine* **37**, 356–
863 365 (2018).
864 33. O'Neill, C., Cassidy, F. C., O'Shea, D. & Hogan, A. E. Mucosal Associated Invariant T Cells in
865 Cancer-Friend or Foe? *Cancers* **13**, 1582 (2021).
866 34. Cao, Y. et al. ER stress-induced mediator C/EBP homologous protein thwarts effector T cell activity
867 in tumors through T-bet repression. *Nat. Commun.* **10**, **12**80 (2019).
868 35. Jin, S. et al. Inference and analysis of cell-cell communication using CellChat. Nat. Commun. 12,
869 1088 (2021).
870 36. Song, K. & Farzaneh, M. Signaling pathways governing breast cancer stem cells behavior. *Stem Cell*
871 *Res. Ther.* **12**, 245 (2021).
872 37. Westermarck, J. & Kähäri, V. Regulation of matrix metalloproteinase expression in tumor invasion.

873 *FASEB J.* **13**, 781–792 (1999).
874 38. Sag, D., Ayyildiz, Z. O., Gunalp, S. & Wingender, G. The Role of TRAIL/DRs in the Modulation of
875 Immune Cells and Responses. Cancers **11**, 1469 (2019).
876 39. Marcheteau, E. et al. Thrombospondin-1 Silencing Improves Lymphocyte Infiltration in Tumors and
877 Response to Anti-PD-1 in Triple-Negative Breast Cancer. Cancers 13, 4059 (2021).
878 40. Kalinina, A. et al. Cyclophilin A is a factor of antitumor defense in the early stages of tumor
879 development. *Int. Immunopharmacol.* **94**, 107470 (2021).
880 41. Charlot, M. et al. Diabetes and breast cancer mortality in Black women. *Cancer Cause Control* **28**,
881 61–67 (2017).
882 **42**. Neal, J. T. et al. Organoid Modeling of the Tumor Immune Microenvironment. Cell **175**, 1972-
883 1988.e16 (2018).
884 43. Mazzucchelli, S. et al. Establishment and Morphological Characterization of Patient-Derived
885 Organoids from Breast Cancer. *Biol Proced Online* **21**, 12 (2019).
886 44. Sachs, N. et al. A Living Biobank of Breast Cancer Organoids Captures Disease Heterogeneity. Cell
887 172, 373-386.e10 (2018).
888 45. Cattaneo, C. M. et al. Tumor organoid–T-cell coculture systems. *Nat Protoc* **15**, 15–39 (2020).
889 46. Meng, Q. et al. Empirical identification and validation of tumor-targeting T cell receptors from
890 circulation using autologous pancreatic tumor organoids. *J. Immunother. Cancer* **9**, e003213 (2021).
891 47. Carolan, E. et al. Altered Distribution and Increased IL-17 Production by Mucosal-Associated
892 Invariant T Cells in Adult and Childhood Obesity. *J. Immunol.* **194**, 5775–5780 (2015).
893 48. He, J., Zhou, Y. & Sun, L. Emerging mechanisms of the unfolded protein response in therapeutic
894 resistance: from chemotherapy to Immunotherapy. *Cell Commun. Signal.* **22**, 89 (2024).
895 **49**. Conza, G. D., Ho, P.-C., Cubillos-Ruiz, J. R. & Huang, S. C.-C. Control of immune cell function by
896 the unfolded protein response. *Nat. Rev. Immunol.* **23**, 546–**562** (2023).
897 50. Chen, X. et al. XBP1 promotes triple-negative breast cancer by controlling the HIF1α pathway.
898 Nature **508**, 103–107 (2014).

899 51. Song, M. et al. IRE1α–XBP1 controls T cell function in ovarian cancer by regulating mitochondrial
900 activity. Nature 562, 423–428 (2018).
901 52. Hurst, K. et al. Endoplasmic Reticulum Stress Contributes to Mitochondrial Exhaustion of CD8 T
902 cells. *Cancer Immunol. Res.* **7**, canimm.0182.2018 (2019).
903 53. Chen, X. & Cubillos-Ruiz, J. R. Endoplasmic reticulum stress signals in the tumour and its
904 microenvironment. Nat. Rev. Cancer 21, 71–88 (2021).
905 54. Donath, M. Y. & Shoelson, S. E. Type 2 diabetes as an inflammatory disease. Nat. Rev. Immunol.
906 **11**, 98–107 (2011).
907 55. Back, S. H. & Kaufman, R. J. Endoplasmic Reticulum Stress and Type 2 Diabetes. *Annu. Rev.*
908 *Biochem.* **81**, 767–793 (2012).
909 56. Bettigole, S. E. & Glimcher, L. H. Endoplasmic Reticulum Stress in Immunity. *Annu. Rev. Immunol.*
910 **33**, 1–31 (2014).
911 57. Eizirik, D. L., Cardozo, A. K. & Cnop, M. The Role for Endoplasmic Reticulum Stress in Diabetes
912 Mellitus. *Endocr. Rev.* **29**, 42–61 (2008).
913 58. Andrieu, G. P. et al. BET proteins in abnormal metabolism, inflammation, and the breast cancer
914 microenvironment. *J Leukocyte Biol* **104**, 265–274 (2018).
915 59. Cortellini, A. et al. Type 2 Diabetes Mellitus and Efficacy Outcomes from Immune Checkpoint
916 Blockade in Patients with Cancer. *Clin. Cancer Res.* **29**, 2714–2724 (2023).
917 60. Kangas, R. et al. Aging and serum exomiR content in women-effects of estrogenic hormone
918 replacement therapy. *Sci. Rep.* **7**, 42702 (2017).
919 61. Drula, R. et al. 17β-estradiol promotes extracellular vesicle release and selective miRNA loading in
920 ERα-positive breast cancer. Proc. Natl. Acad. Sci. **120**, e2122053120 (2023).
921 62. Zanini, B. M. et al. Dynamics of serum exosome microRNA profile altered by chemically induced
922 estropause and rescued by estrogen therapy in female mice. *GeroScience* **46**, 5891–5909 (2024).
923 63. Schindelin, J. et al. Fiji: an open-source platform for biological-image analysis. *Nat. Methods* **9**,
924 676–682 (2012).

925 64. Hao, Y. et al. Dictionary learning for integrative, multimodal and scalable single-cell analysis. Nat.
926 Biotechnol. 42, 293–304 (2024).
927 65. Choudhary, S. & Satija, R. Comparison and evaluation of statistical error models for scRNA-seq.
928 *Genome Biol.* **23**, 27 (2022).
929 66. Luecken, M. D. et al. Benchmarking atlas-level data integration in single-cell genomics. Nat.
930 Methods **19**, 41–50 (2022).
931 67. Patel, A. P. et al. Single-cell RNA-seq highlights intratumoral heterogeneity in primary
932 glioblastoma. Science **344**, 1396–1401 (2014).
933 68. Finak, G. et al. MAST: a flexible statistical framework for assessing transcriptional changes and
934 characterizing heterogeneity in single-cell RNA sequencing data. Genome Biol. **16**, 278 (2015).
935 69. Ru, Y. et al. The multiMiR R package and database: integration of microRNA–target interactions
936 along with their disease and drug associations. Nucleic Acids Res. 42, e133–e133 (2014).
937 70. Reed, E. R. & Monti, S. Multi-resolution characterization of molecular taxonomies in bulk and
938 single-cell transcriptomics data. Nucleic Acids Res. 49, e98–e98 (2021).